Roles of Mesoscale Eddies in the Kuroshio Paths

YASUMASA MIYAZAWA

Frontier Research System for Global Change/JAMSTEC, Yokohama City, Kanagawa, Japan

XINYU GUO

Frontier Research System for Global Change/JAMSTEC, Yokohama City, Kanagawa, Japan, and Center for Marine Environmental Studies, Ehime University, Matsuyama, Japan

TOSHIO YAMAGATA

Frontier Research System for Global Change/JAMSTEC, Yokohama City, Kanagawa, Japan, and Department of Earth and Planetary Science, Graduate School of Science, The University of Tokyo, Tokyo, Japan

(Manuscript received 11 June 2002, in final form 8 April 2004)

ABSTRACT

A high-resolution ocean general circulation model is developed to simulate connections between the Kuroshio path variations and mesoscale eddy activities as realistically as possible. The climatological mean of the modeled Kuroshio takes a nearshore nonlarge meander path. It is found that the model is capable of simulating two types of nonlarge meander state and a possible version of the large meander state. The offshore nonlarge meander is generated through interaction between the Kuroshio and an anticyclonic eddy. The large meander occurs just after significant intensification of the anticyclonic Kuroshio recirculation; successive intrusion of anticyclonic eddies from the upstream region is responsible for this process. Those anticyclonic eddies are advected by the Kuroshio from the region northeast of Luzon Island and increase the upstream Kuroshio volume transport on an interannual time scale. The cyclonic eddies propagating from the Kuroshio Extension region, on the other hand, weaken the Kuroshio meander after the merger. The Kuroshio path variations south of Japan thus seem to be closely related to eddy activities in the subtropical gyre system.

1. Introduction

The Kuroshio is one of the most energetic western boundary currents associated with high mesoscale eddy activity. It is unique among various western boundary currents in that the Kuroshio has three typical paths along the southern coast of Japan. As shown in Fig. 1, these are the large meander path, the nearshore nonlarge meander path, and the offshore nonlarge meander path according to the definition given by Kawabe (1985). The large meander and nonlarge meander paths persist from a few years to a decade, suggesting a link with basinwide climate variations. The large meander path has not been observed during the last decade. However, the transition between the nearshore nonlarge meander path and the offshore nonlarge meander path has been frequently observed; the primary period of the path transition is 1.6–1.8 yr (Kawabe 1987).

Recent studies suggest that the transition between the nearshore and the offshore nonlarge meander paths during the last decade is influenced by mesoscale eddy activity (Ebuchi and Hanawa 2000, 2003; Mitsudera et al. 2001). Analyzing satellite altimetry data, Ebuchi and Hanawa (2003) suggested that anticyclonic/cyclonic eddies trigger the offshore nonlarge meander observed from 1993 to 1999. Several numerical experiments have been performed recently to examine how an anticylonic eddy inserted artificially in ocean models triggers the path transition from the nearshore to the offshore nonlarge meander path (Mitsudera et al. 2001) or to the large meander path (Endoh and Hibiya 2001; Akitomo and Kurogi 2001). However, the inflow/outflow models (Mitsudera et al. 2001; Endoh and Hibiya 2001) or noneddy-resolving models (e.g., Akitomo and Kurogi 2001) cannot capture the mesoscale eddy activity linked to basin-scale processes.

Recent observational studies suggest that two kinds of mesoscale eddy activity exist in this region. The first is westward-propagating eddies with a spatial scale of 500 km and a time scale less than 3 months, probably originating in the Kuroshio Extension and entering the Kuroshio recirculation region at 30°N (Ebuchi and Han-

Corresponding author address: Yasumasa Miyazawa, Frontier Research System for Global Change/JAMSTEC, 3173-25 Showamachi, Kanazawa-ku, Yokohama City, Kanagawa 236-0001, Japan.
E-mail: miyazawa@jamstec.go.jp

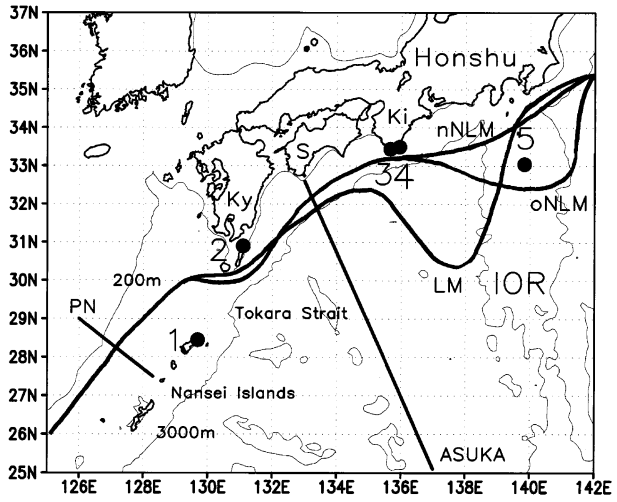

FIG. 1. Tide gauge stations and typical paths (LM: large meander path, oNLM: offshore nonlarge meander path, and nNLM: nearshore nonlarge meander path) of the Kuroshio. The numbers denote the tide stations and the abbreviations represent locations (1: Naze, 2: Nishinoomote, 3: Kushimoto, 4: Uragami, 5: Hachijojima, Ki: Kii Peninsula, S: Shikoku, Ky: Kyushu, and IOR: Izu–Ogasawara Ridge). We note that Uragami (4) is located slightly downstream of Kushimoto (3). Labels PN and ASUKA denote the CTD line of the Nagasaki Marine Observatory and the line of the ASUKA observation group, respectively.

awa 2000). The second is mesoscale eddies located farther to the south near 23°N. After being captured by the offshore current of the Kuroshio south of Okinawa (the Ryukyu Current), they are advected by the Kuroshio itself to the Shikoku Basin, where they eventually merge with the eddies mentioned above (Ichikawa 2001).

Many theoretical works have addressed mechanisms of the Kuroshio large meander since the pioneering work of Robinson and Taft (1972) (see references of Qiu and Miao 2000). Using an eddy-permitting, two-layer primitive equation model of the North Pacific Ocean, Qiu and Miao (2000) have recently suggested that the accumulation of low potential vorticity water in the Kuroshio recirculation region influences the Kuroshio path variation. They renewed interest in possible connections of the Kuroshio large meander to the whole subtropical gyre system including the low latitudes as well as the recirculation region, rather than considering the meander simply as a local nonlinear phenomenon (see also Saiki 1982; Yamagata et al. 1985; Yamagata and Umatani 1987). Hurlburt et al. (1996), using an eddy-resolving, six-layer primitive equation model, also showed that the basinwide structure of stratification and the basinwide increasing/decreasing trend of the wind stress change the frequency of the large meander path through baroclinic instability west of the Izu–Ogasawara Ridge. However, the explicit roles of the mesoscale eddies south of Japan have not been clarified so far using a basin-scale ocean general circulation model (OGCM).

The purpose of this paper is to investigate possible connections between the Kuroshio path variations and mesoscale eddy activity using an eddy-resolving OGCM. The horizontal grid spacing of the model is $\frac{1}{12}^\circ$ in both zonal and meridional directions, which corresponds to about 9 km in the Kuroshio region. This grid spacing is much smaller than the first baroclinic Rossby radius in the Northwest Pacific (see Emery et al. 1984). The present model with forcing from 1992–1998 reproduces the offshore nonlarge meander path, the nearshore nonlarge meander path, and a possible version of the large meander path.

This paper is organized as follows. In section 2, the model configuration is described. In section 3, the mean state and variability of the model are discussed. Then sea level variations are discussed in connection with the Kuroshio path variation. The model skill for representing mesoscale eddy activities is also argued. In section 4, we describe details of the Kuroshio path variation in view of the interaction with mesoscale eddies. We also examine effects of the mesoscale eddy activity on the intensity of the Kuroshio. Section 5 is devoted to summary and discussion.

2. Numerical model

The present model is based on one of the world community models, the Princeton Ocean Model (POM; Mellor 1996). The POM is a three-dimensional primitive equation ocean model including thermodynamics. The vertical coordinate of the POM is represented by a bottom-following (sigma coordinate) system. The horizontal grids are defined on spherical coordinates. The vertical viscosity and diffusivity are calculated using the Mellor and Yamada (1982) level-2.5 turbulent closure scheme. The horizontal viscosity is calculated by the Smagorinsky-type formulation (Smagorinsky et al. 1965), which is proportional to the square of grid size and horizontal velocity shear with a coefficient of 0.05. The horizontal diffusivity coefficient is assumed to be one-half of the viscosity coefficient. The bottom stress is calculated by the quadratic formula with an empirical drag coefficient, the minimum value of which is 2.5×10^{-3}. Coastal boundary conditions are no slip as well as no mass flux.

The model for the North Pacific (Fig. 2) is run in both low-resolution ($\frac{1}{4}^\circ$–1°) and high-resolution ($\frac{1}{12}^\circ$) configurations. The bottom topography of the low-resolution model is created from the $\frac{1}{12}^\circ$ global height data, GETECH DTM5. This low-resolution basinwide model ranges from 30°S to 62°N and from 100°E to 70°W and has 21 sigma levels in the vertical direction as in the previous study (Guo et al. 2001). The horizontal resolution varies from $\frac{1}{4}^\circ$ in the region corresponding to the high-resolution model to 1° near the boundary. The high-resolution regional model, with uniform horizontal resolution of $\frac{1}{12}^\circ$, extends from 10° to 50°N and from 117°E to 180° (Fig. 2). This high-resolution model has 45 sigma levels (Table 1). The distribution of vertical levels is introduced to resolve the bottom and surface

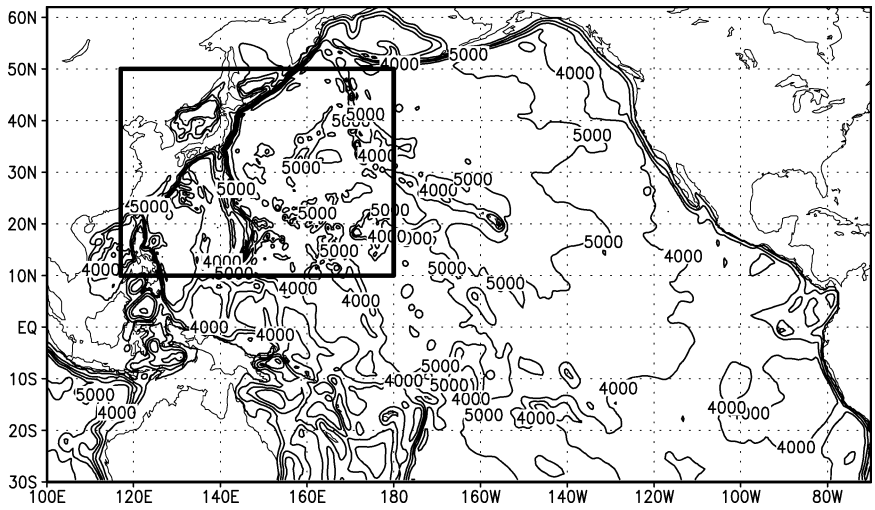

FIG. 2. Bottom topography. The nested area is indicated with a rectangle.

boundary layers. The bottom topography of the high-resolution model is also created from the $\frac{1}{12}^\circ$ data, DTM5. In addition, the 500-m mesh bottom topography provided by Hydrographic Department of Japan is embedded in the coastal sea around Japan.

The bottom topography in both models has been smoothed to reduce the pressure gradient error (Mellor et al. 1994). The maximum bottom slope between two adjacent grid points is constrained by the inequality, $(|H_1 - H_2|)/(|H_1 + H_2|) \leq 0.2$. To reduce the pressure gradient error, we have adopted a Gaussian smoother with ½° scale for the low-resolution grid and with $\frac{1}{12}^\circ$ scale for the high-resolution grid. A ''zero forcing run'' with a horizontally uniform, stable stratification allows us to estimate the current induced by the pressure gradient error. The magnitude of the erroneous velocity due to the pressure gradient error is less than a few centimeters per second for both of the models. We note here that local topography such as the Koshu Seamount, which may influence the Kuroshio path dynamics south of Japan (Hurlburt et al. 1996; Endoh and Hibiya 2001), is well resolved in the high-resolution model even after the smoothing.

TABLE 1. Sigma coordinate used in the high-resolution model.

Layers	Sigma coordinate	Layers	Sigma coordinate
1	0.000	24	−0.275
2	−0.002	25	−0.300
3	−0.005	26	−0.325
4	−0.010	27	−0.350
5	−0.015	28	−0.375
6	−0.025	29	−0.425
7	−0.035	30	−0.475
8	−0.045	31	−0.525
9	−0.055	32	−0.575
10	−0.065	33	−0.625
11	−0.075	34	−0.675
12	−0.085	35	−0.725
13	−0.095	36	−0.775
14	−0.105	37	−0.825
15	−0.120	38	−0.875
16	−0.135	39	−0.900
17	−0.150	40	−0.925
18	−0.165	41	−0.950
19	−0.180	42	−0.970
20	−0.195	43	−0.980
21	−0.210	44	−0.990
22	−0.225	45	−1.000
23	−0.250		

Northern and southern boundaries of the low-resolution model are treated as open boundaries, along which a radiation condition is adopted on external mode velocities, together with a one-sided advection scheme for temperature and salinity. Both temperature and salinity fields are specified on open boundaries using monthly climatology data (Levitus and Boyer 1994; Levitus et al. 1994). The internal-mode velocities on open boundaries are assumed to vanish.

Variables on all lateral boundaries of the high-resolution regional model are determined by values interpolated bilinearly from the low-resolution basin model (Guo et al. 2003). Vertical boundary variables for the high-resolution model with 45 sigma levels are created from the low-resolution model with 21 sigma levels by linear interpolation. The radiation condition considering the sea surface height of the lower-resolution model is adopted on external mode velocities to keep calculation stable. Daily mean variables of the low-resolution model are stored on a disk for the purpose of one-way nesting. The bottom topography near the boundary of the high-resolution model is the same as that of the low-resolution model to allow a smooth connection of both models by linear interpolation of sigma coordinate variables.

Sea ice formation and river runoff are not included in these simulations. Since nudging to the monthly climatology of temperature and salinity in the Okhotsk Sea improves watermass properties in the mixed water

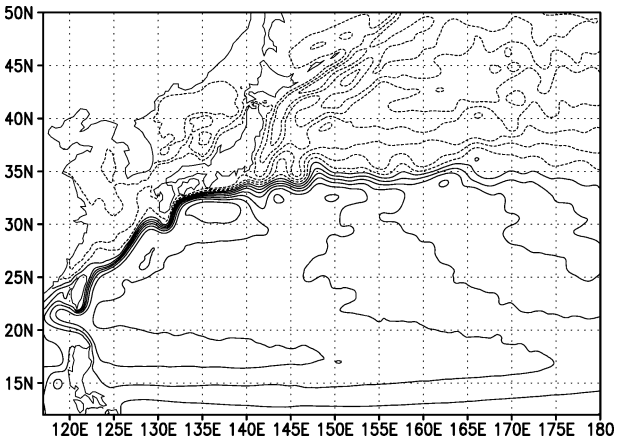

FIG. 3. Mean sea surface height of the model from 1992 to 1998. Contour interval is 0.1 m.

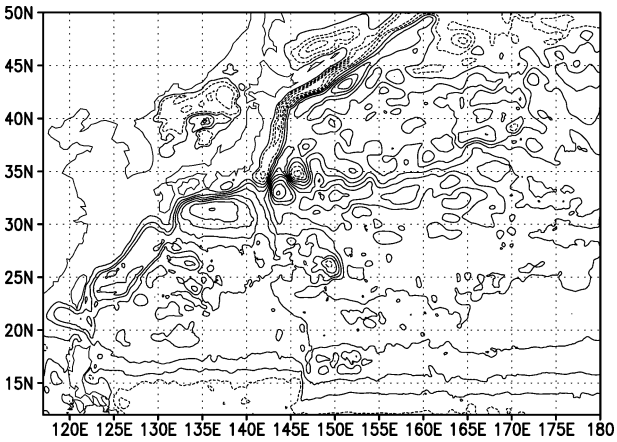

FIG. 4. Mean streamfunction of the model from 1992 to 1998. Contour interval is 10 Sv.

region north of the Kuroshio Extension (H. Mitsudera 2000, personal communication), we followed their recipe in both the Okhotsk Sea and the Bering Sea. This procedure may be regarded as a kind of parameterization for sea ice and lateral freshwater effects. The sea surface temperature is nudged to the observed temperature with a restoring time scale of 7 days in both regions.

The model is driven by wind stresses and heat and salt fluxes. The wind stress field is calculated on a weekly basis from *ERS-1* and *-2* (European Remote Sensing Satellite) scatterometer data with a $1^\circ \times 1^\circ$ resolution. The Reynolds and Smith (1994) sea surface temperature field used in the simulation is blended from ship, buoy, and bias-corrected satellite data with a $1^\circ \times 1^\circ$ resolution also on a weekly basis. The surface heat flux is applied using the Haney-type formula (Haney 1971); the coefficient used in the retroaction term is 35 W m^{-2} K^{-1}. Salinity at the surface is restored to the monthly mean climatology (Levitus et al. 1994) with a time scale of 30 days.

The present simulation is conducted with two steps: an initial spinup experiment and an experiment with forcing from 1992 to 1998. In the spinup experiment, the two models are started from a state of rest with annual-mean temperature and salinity derived from the $\frac{1}{4}^\circ \times \frac{1}{4}^\circ$ climatology data (Boyer and Levitus 1997). The spinup period is 20 years for the coarse-resolution model and 12 years for the fine-resolution model. They are forced by monthly mean climatological wind stresses derived from *ERS-1* and *-2* wind data and monthly mean climatological heat flux (Da Silva et al. 1994) modified with the monthly mean SST data. The simulation used for the present analysis is started from the final year of the spinup experiment using the weekly mean wind stress and the monthly mean climatological heat flux modified with the weakly mean SST data from 1 January 1992 to 31 December 1998.

3. The model results

a. Mean state of the Kuroshio

Figure 3 shows the mean sea surface height field from the high-resolution model during the simulation period from 1992 to 1998. The model reproduces the Kuroshio–Kuroshio Extension system well with a reasonable separation latitude at around 35°N. In addition, the anticyclonic recirculation gyre is resolved on the southern side of the Kuroshio, which is comparable to the observed recirculation (e.g., Hasunuma and Yoshida 1978). We also note that the model climatology of the Kuroshio path south of Japan is the nearshore nonlarge meander path.

The streamfunction averaged for the period from 1992 through 1998 is shown in Fig. 4. The volume transport of the Kuroshio across the PN line in the East China Sea (see Fig. 1) and that for the Ryukyu Current east of the Nansei Islands are about 25 and 15 Sv (Sv $\equiv 10^6$ m^3 s^{-1}), respectively, which are comparable to observations (Kawabe 1995; Zhu et al. 2003). Therefore, the present model resolves successfully the two upstream branches of the Kuroshio. However, the eastward volume transport across the ASUKA line south of Japan (Fig. 1) reaches 79 Sv, which is much larger than the mean value of 57 Sv observed from 1992 to 1997 by Imawaki et al. (2001). The volume transport associated with the Kuroshio Countercurrent is about 39 Sv in the model while the corresponding volume transport south of Shikoku is only 15 Sv in the observation.

b. Variability of the surface geostrophic current

In order to examine ocean variability near the surface, the eddy kinetic energy (EKE) field derived from satellite altimetry data such as Ocean Topography Experiment (TOPEX)/Poseidon (T/P) is quite useful. Because of their global coverage, satellite data effectively capture the spatial pattern of eddy activity (Stammer 1997).

In the present study, we use the National Aeronautics and Space Administration Goddard Space Flight Center Ocean Pathfinder collinear dataset for the T/P altimeter mission over the period between September 1992 and December 1998.

The EKE is calculated from the along-track gradient in the sea surface height anomaly, assuming the geostrophic approximation. Before this calculation, the model sea surface height anomaly is interpolated on the satellite track. Then the EKE along the satellite track is interpolated to half-degree regular grids using an optimal interpolation method.

Figure 5a shows that the satellite-derived EKE is higher than 0.03 $m^2\ s^{-2}$ in the western subtropical region between 15° and 40°N. In particular, the North Equatorial Current and the Kuroshio–Kuroshio Extension show values higher than 0.08 $m^2\ s^{-2}$. The flow field south of Japan also shows high EKE, which reflects the path variation of the Kuroshio. As shown in Fig. 5b, the present high-resolution model successfully reproduces those satellite-derived features. The maximum EKE in the Kuroshio–Kuroshio Extension region is larger than 0.3 $m^2\ s^{-2}$ in the model, which is comparable to the observation. The high EKE in the Kuroshio region is attributed not only to mesoscale eddy activity but also to the path migration of the Kuroshio (Mizuno and White 1983). The present model succeeds in representing such variability as well. The realistic EKE distribution in the model mainly results from the high horizontal resolution (Guo et al. 2003). However, the model does not reproduce well the observed EKE in the central part of the subtropical gyre. This may reflect the deficiency of resolving midocean eddies in the low-resolution model.

c. Mesoscale eddy activity south of Japan

Ebuchi and Hanawa (2000) have reported significant mesoscale eddy activity with a time scale of 40–200 days south of Japan (27°–30°N, 135°–155°E) using the T/P data. In a subsequent paper, they have suggested that coalescence of the mesoscale eddy with the main stream may trigger the path variation of the Kuroshio (Ebuchi and Hanawa 2003).

In order to compare statistical properties of the eddy activity with observations, we plot the power spectra of sea surface height anomaly calculated using the T/P data and the model output (Fig. 6). Although the model fails to simulate the eddy activity with time scales of 40–200 days south of Japan (27°–30°N, 135°–155°E), it successfully simulates the eddy activity in a slightly more northern region (29°–32°N, 135°–155°E). The horizontal scale evaluated from the filtered sea surface height anomaly in the latter region is 500 km, which is comparable with the observation. The westward phase speed estimated from the model result is 5.5 cm s^{-1}, which is almost the same as the observed value of 5.4 cm s^{-1}. The vertical sections for simulated eddies over the Izu–Ogasawara Ridge are shown in Fig. 7. The eddy has a diameter of about 400 km and a maximum swirling speed of about 60 cm s^{-1} and extends to a depth of 1000 m. Displacement of the 15°C isotherm reaches about 200 m at the center. All of these properties correspond well to observations (Ebuchi and Hanawa 2000; Mitsudera et al. 2001).

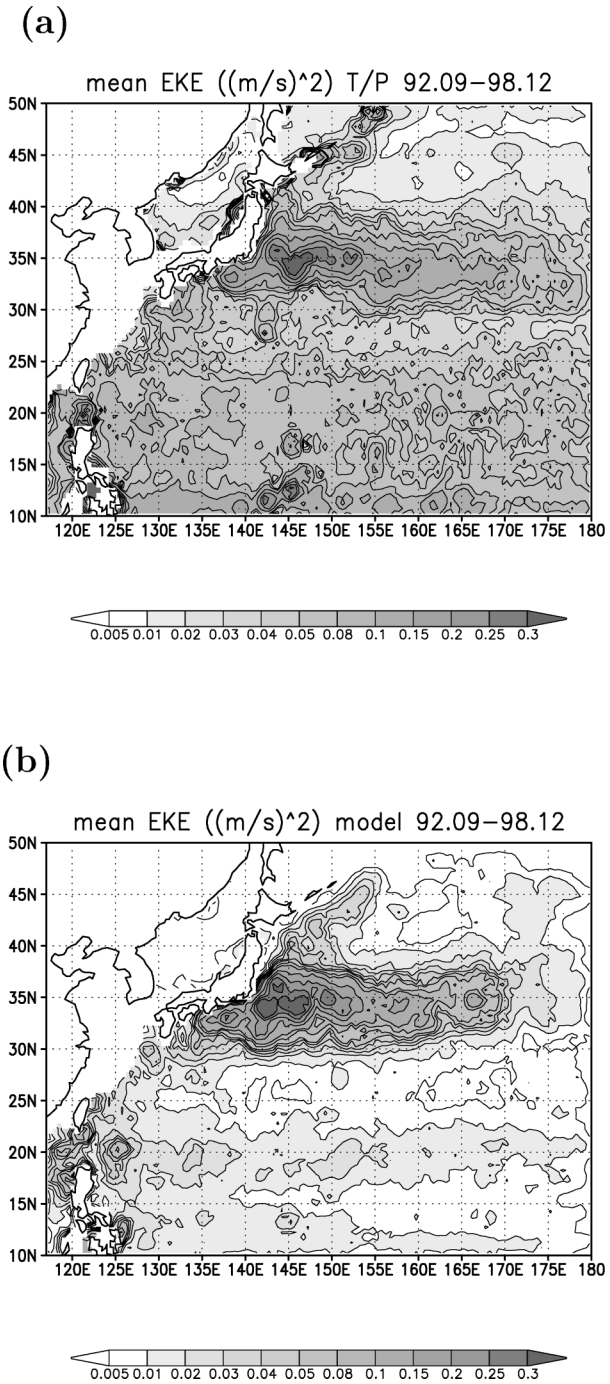

FIG. 5. Mean eddy kinetic energy ($m^2\ s^{-2}$) calculated from sea surface height anomaly (Sep 1992–Dec 1998): (a) TOPEX/Poseidon altimetry and (b) model result.

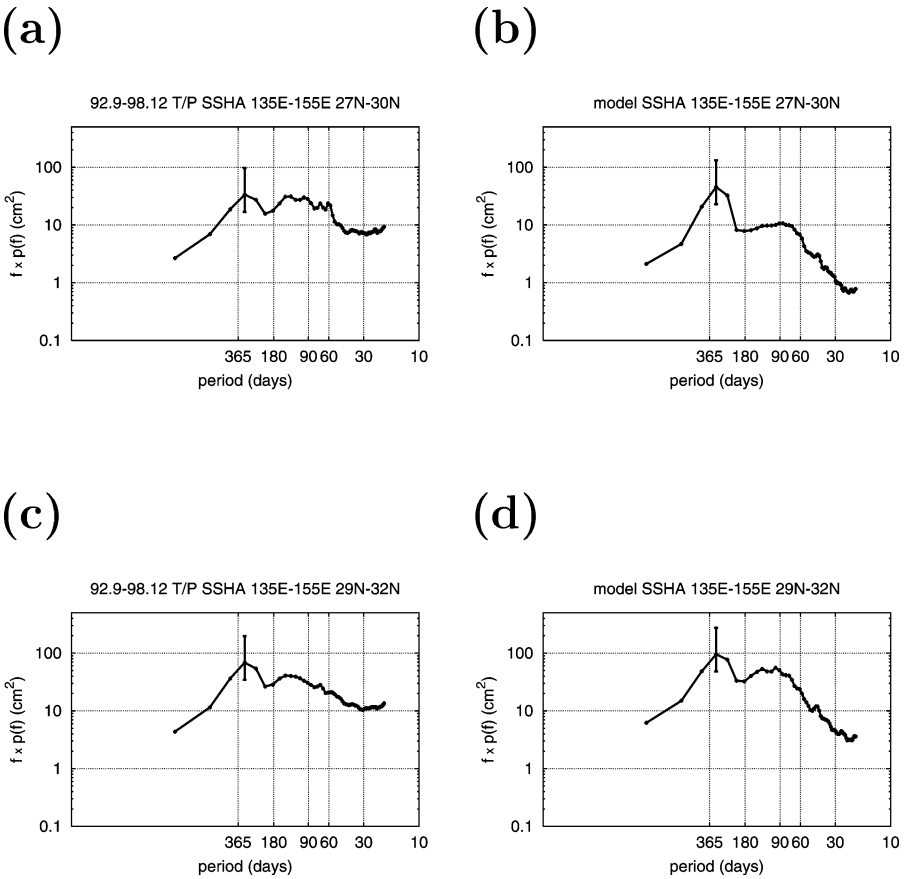

FIG. 6. Power spectra of sea surface height anomaly. (a) TOPEX/Poseidon data averaged in the region (27°–30°N, 135°–155°E), (b) the model result averaged in the region (27°–30°N, 135°–155°E), (c) TOPEX/Poseidon data averaged in the region (29°–32°N, 135°–155°E), and (d) the model result averaged in the region (29°–32°N, 135°–155°E). An error bar indicating 95% confidence level is shown in each panel.

d. Path variations of the Kuroshio

Three different types of the Kuroshio path south of Japan are simulated in the present model, which uses forcing from January 1992 to December 1998. Two correspond to the nearshore nonlarge meander and the offshore nonlarge meander, following the definition of Kawabe (1985). The other path is similar to the large meander. The mean path during the simulation period corresponds to the nearshore nonlarge meander path (Fig. 3).

It is well known that the change of the Kuroshio path is associated with sea level changes along the southern coast of Japan. According to tide gauge data, the sea level difference between Kushimoto and Uragami (see Fig. 1 for locations) during the large meander state is negative (about −10 mm) and less variable than during the nonlarge meander state (Kawabe 1995). As shown in Fig. 8a, this feature is reproduced well in the present model. The modeled Kuroshio path from November 1993 to July 1994 and from January 1998 to May 1998 is similar to the large meander path. The sea level difference between Kushimoto and Uragami is negative and less variable during these periods as in the observations, even though the duration is much shorter than is observed. The actual large meander path persists for a period from a few years to a decade. On the other hand, the real Kuroshio shows only transitions between the offshore and nearshore nonlarge meander paths during the simulation period (Ebuchi and Hanawa 2003).

Kawabe (1985) showed that the sea level at Hachijojima (see Fig. 1 for location) is useful for distinguishing the offshore nonlarge meander from the nearshore nonlarge meander. When the sea level at Hachijojima is high, the main axis of the Kuroshio is close to the Japan coast. On the other hand, when the sea level at Hachijojima is low, the Kuroshio is away from the coast of Honshu. The time series of the model sea level at Hachijojima indicates the existence of two basic states. The nearshore nonlarge meander is characterized by sea level ranging from 0 to 400 mm and the offshore nonlarge meander is for the range from −700 to −300 mm (see arrows in Fig. 8b). Thus the model appears to re-

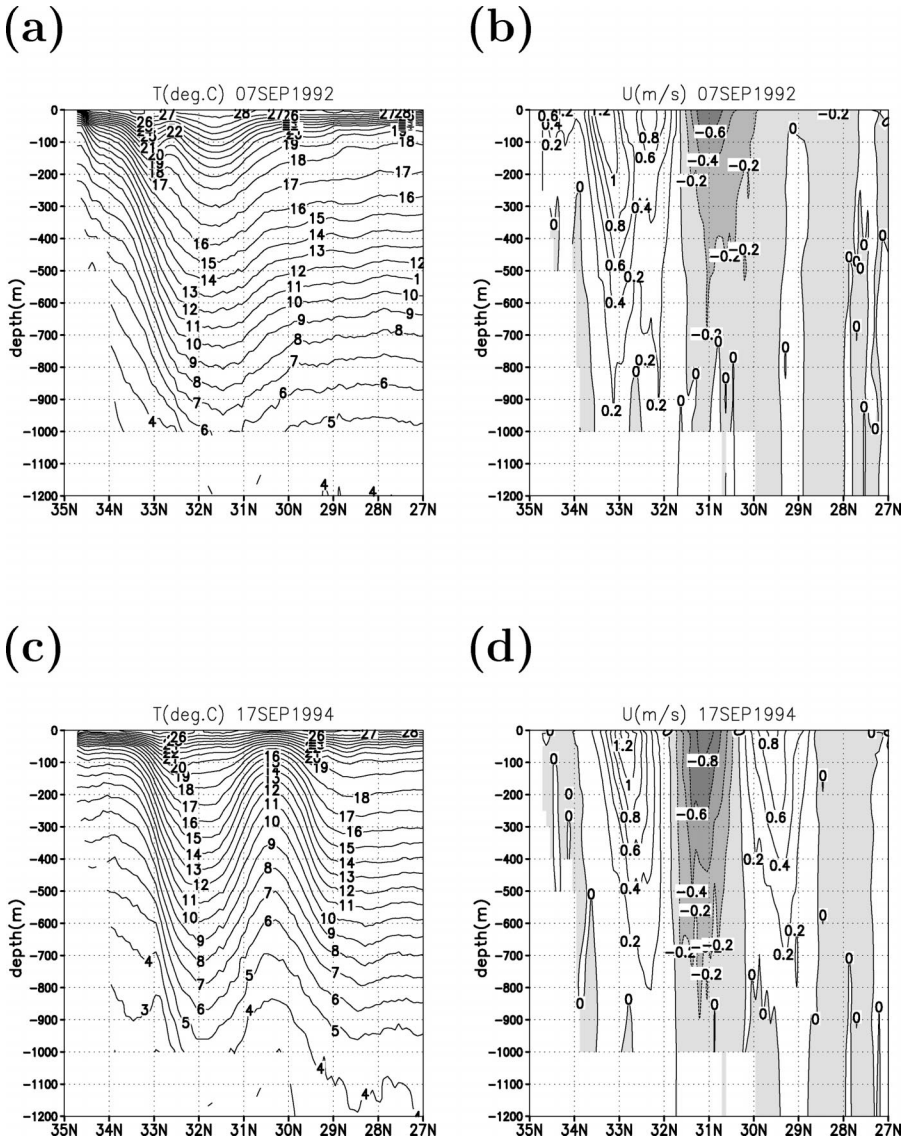

FIG. 7. Depth–latitude sections at 139°E. (a) Temperature and (b) eastward velocity of a simulated anticyclonic eddy on 7 Sep 1992. (c) Temperature and (d) eastward velocity of a simulated cyclonic eddy on 17 Sep 1994. Contour interval of temperature is 1°C and that of velocity is 0.2 m s^{-1}.

produce both nonlarge meander paths during the simulation period. We note that a low sea level state at Hachijojima in the model appears to correspond to the state of negative sea level difference between Kushimoto and Uragami. This feature is inconsistent with observation; the typical large meander shows high sea level state at Hachijojima (Kawabe 1985).

In summary, the model reasonably reproduces both of the two nonlarge meander states, but its ability to reproduce the large meander state needs improvement because the duration is too short in comparison with observations. The low sea level state at Hachijojima, which has been frequently observed in the decay phase of the large meander (Kawabe 1995), may be associated with the short duration of the large meander in the present model. Nevertheless, the existence of the brief large meander states in the model is worthy of further investigation; the present model appears to capture almost all key elements in the Kuroshio path dynamics.

4. Roles of mesoscale eddies on the Kuroshio path variations

a. Offshore nonlarge meander

The sea level at Hachijojima exhibits a low state for a short period of about 1 month three times from February 1993 to August 1993 (see arrows in Fig. 8b). These short-term variations correspond to the offshore nonlarge meander as mentioned in the previous section. We analyze the process here in detail.

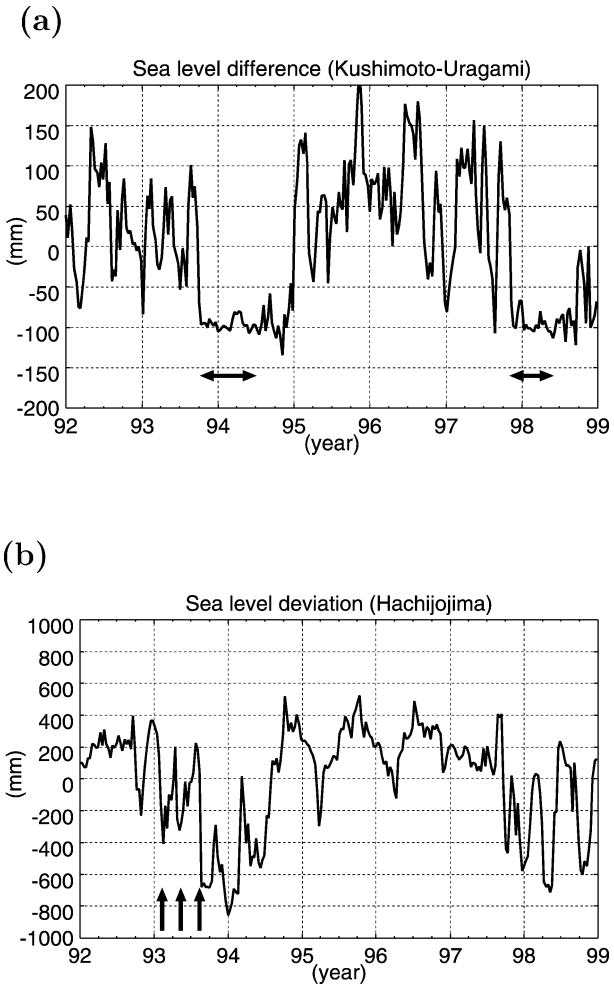

FIG. 8. (a) Time series of model sea level difference between Kushimoto and Uragami. Lines with arrows denote the large meander period. (b) Time series of model sea level at Hachijojima. Both data are averaged over 10 days, and the reference value is the mean for the period from Jan 1992 to Dec 1998. The arrows denote the onset of the offshore nonlarge meander path.

As shown in Fig. 9a, small anticyclonic eddies are found along the offshore side of the Kuroshio from the Luzon Island to the Kuroshio recirculation region in summer 1992. Anticyclonic eddies passing through the Tokara Strait influence the Kuroshio path there and induce subsequent small meanders farther downstream southeast of Kyushu. Ichikawa (2001) has discussed the phenomenon using the T/P, *ERS-1,* and *ERS-2* altimetry data. The small anticyclonic eddies propagating downstream are absorbed by a large anticyclonic eddy located near the Izu–Ogasawara Ridge. The large eddy then propagates westward and collides with the Kuroshio east of Kyushu about 3 months after the eddy formation (Fig. 9b). The Kuroshio is intensified in this way and then meanders east of the Kii Peninsula in February of 1993 (Fig. 9c). This eddy–Kuroshio interaction process is similar to a real event observed in 1998 (Mitsudera et al. 2001; Ebuchi and Hanawa 2003). The anticyclonic eddy associated with this offshore nonlarge meander evolves by absorbing small eddies near the Izu–Ogasawara Ridge and finally separates from the Kuroshio. Then the whole process is repeated two more times (e.g., Fig. 9d).

b. Large meander

The Kuroshio followed the large meander path after three episodes of interaction with an anticyclonic eddy during the state of the offshore nonlarge meander as described in section 4a. The large meander thus generated is associated with negative sea level difference between Kushimoto and Uragami from November 1993 to July 1994 (Fig. 8a). The anticyclonic eddy, indicated by the arrow in Fig. 10a, starts moving westward. Then the eddy collides with the Kuroshio (Fig. 10b) and is advected back eastward by the current. Associated with this process, the large meander grows southeast of the Kii Peninsula (Figs. 10b–d). This large meander is strengthened by absorbing a cyclonic eddy east of the Izu–Ogasawara Ridge and then sheds a strong eddy, that is, a cyclonic ring. This results in a nearshore nonlarge meander path (not shown).

The second large meander occurs suddenly in January 1998 (Fig. 11). The weak cyclonic eddy south of Shikoku is first captured by the Kuroshio, as indicated by the arrow in Fig. 11a. The meander southeast of the Kii Peninsula grows just after that, as shown in Figs. 11b–d. The second large meander also absorbs the cyclonic eddy east of the Izu–Ogasawara Ridge, and then moves toward the east of the Izu–Ogasawara Ridge and returns to the nonlarge meander (not shown).

In order to analyze the meander growth, the vertical velocity at 400-m depth and the abyssal flow at 4000-m depth are shown for the two large-meander cases and for one nonlarge meander case (Fig. 12). Large anomalous downward velocity is found in the east half of the meander trough, whereas anomalous upward velocity is found in the west half. Abyssal anticyclonic circulation exists below the upper downwelling region. Cyclonic circulation occurs at middepth (2000–3000 m) below the upwelling region (not shown). These features are consistent with the dynamical constraint of potential vorticity conservation. The large meander path (Figs. 12a,b) is associated with the strengthened abyssal anticyclonic circulation around Koshu Seamount and shows a contrast to the offshore nonlarge meander path (Fig. 12c), as previously simulated by Hurlburt et al. (1996) and Endoh and Hibiya (2001).

Figure 13 shows the kinetic energy at 4000-m depth averaged in 31.5°–32.5°N, 132°–137°E. There are four peaks ($>0.4 \times 10^{-4}$ m^2 s^{-2}) during the simulation period. Three of them correspond to the large meander paths and are indicated by arrows. The fourth peak, in October 1994, is due to passage of the cyclonic eddy through the analysis region. The offshore nonlarge me-

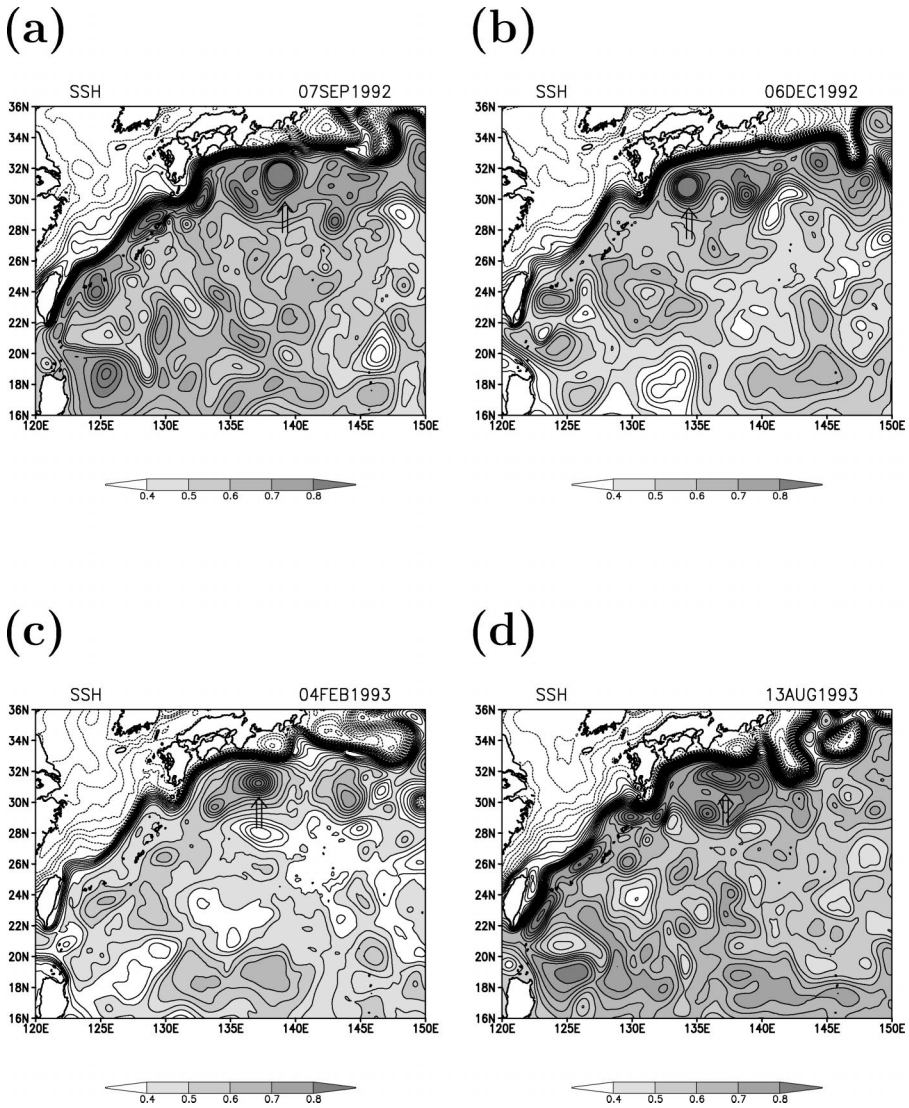

FIG. 9. Evolution of sea surface height showing the interaction of the anticyclonic eddy (indicated by arrows) and the Kuroshio. Contour interval is 0.05 m. Regions greater than 0.6 m are shaded: (a) 7 Sep 1992, (b) 6 Dec 1992, (c) 4 Feb 1993, and (d) 13 Aug 1993.

ander (e.g., the peak on 13 August 1993) is associated with much smaller kinetic energy. The marked rise in the abyssal kinetic energy during the onset phase of the large meander path suggests vertical kinetic energy transfer due to baroclinic instability. In section 4c, we address the energetics of the meander growth.

c. Energetics of the meander growth

To examine how the large meander grows, we have analyzed local energetics in a way similar to Masina et al. (1999) and Wells et al. (2000). The results are also compared with a standard linear stability analysis to clarify mechanisms of the initial growth. Although the simulated large meanders are short lived as compared with the observed phenomena, the present analysis is useful in understanding the genesis of the large meander.

The local energy transfer from mean kinetic energy to eddy kinetic energy is expressed as follows (Wells et al. 2000):

$$K = -\left[\overline{u'u'}\frac{\partial \overline{u}}{\partial x} + \overline{u'v'}\left(\frac{\partial \overline{u}}{\partial y} + \frac{\partial \overline{v}}{\partial x}\right) + \overline{v'v'}\frac{\partial \overline{v}}{\partial y}\right], \quad (1)$$

where $\overline{u}(\overline{v})$ is the eastward (northward) mean velocity and $u'(v')$ is the eastward (northward) perturbed velocity. When K is positive, the barotropic energy transfer may generate disturbances. Similarly, the energy transfer from mean potential energy to eddy kinetic energy is judged by the following term:

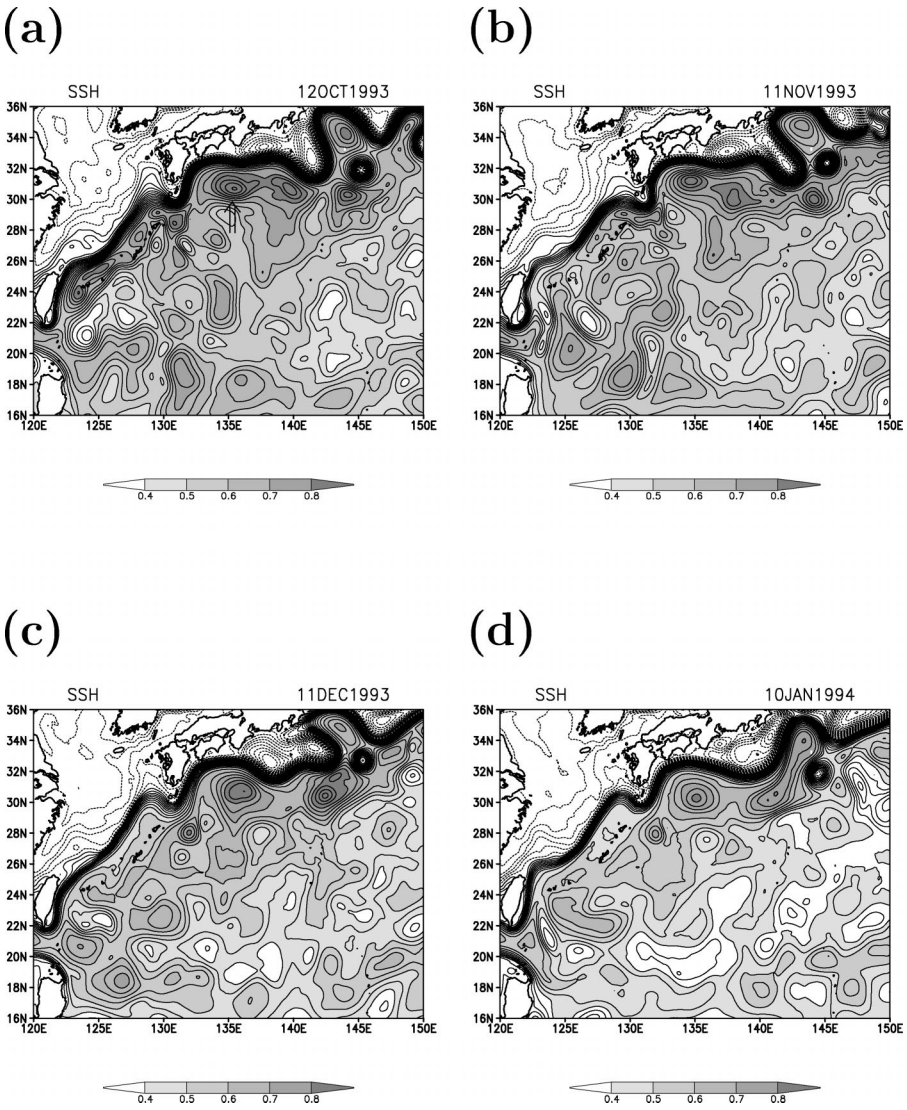

FIG. 10. As in Fig. 9 except showing the amplification of the Kuroshio meander due to the interaction with the anticyclonic eddy [indicated by an arrow in (a)]: (a) 9 Feb 1994, (b) 1 Mar 1994, (c) 21 Mar 1994, and (d) 10 Apr 1994.

$$P = -g\frac{\overline{u'\rho'}(\partial\overline{\rho}/\partial x) + \overline{v'\rho'}(\partial\overline{\rho}/\partial y)}{d\rho_b/dz}, \qquad (2)$$

where g is the gravity acceleration, and ρ', $\overline{\rho}$, and $\rho_b(z)$ are the perturbed, mean, and background density fields. When P is positive, the baroclinic energy transfer may generate disturbances. A part of P is transformed into eddy kinetic energy through the buoyancy term, $B = -g\overline{\rho' w'}$, where w' is the perturbed vertical velocity. However, the complicated distribution of vertical velocity due to rough bottom topography prevents us from obtaining a meaningful view from the plot of B (Wells et al. 2000).

Figure 14a shows a meridional section at 136°E of the time-averaged eddy kinetic energy $(\overline{u'^2} + \overline{v'^2})/2$ during the period when the first meander grows. We find two peaks: one is at the Kuroshio core of the nonlarge meander path (33°N) and another is on the offshore side of the Kuroshio (32.2°N). Meridional sections of the conversion terms K at 136°E (Fig. 14b) show two positive K regions (on the onshore side at 33.7°N and on the offshore side at 32.7°N) within the upper 300 m. On the other hand, the maximum of P is found in the Kuroshio core near 33°N (Fig. 14c). This corresponds to the maximum of the eddy kinetic energy on the onshore side (Fig. 14a). We also note that the positive P region extends to the main thermocline at 600-m depth. This suggests that the evolving cyclonic disturbance due to baroclinic instability may influence the movement of the Kuroshio core of the nonlarge meander path during the onset phase of the large meander path. Barotropic instability appears to be responsible for further growth

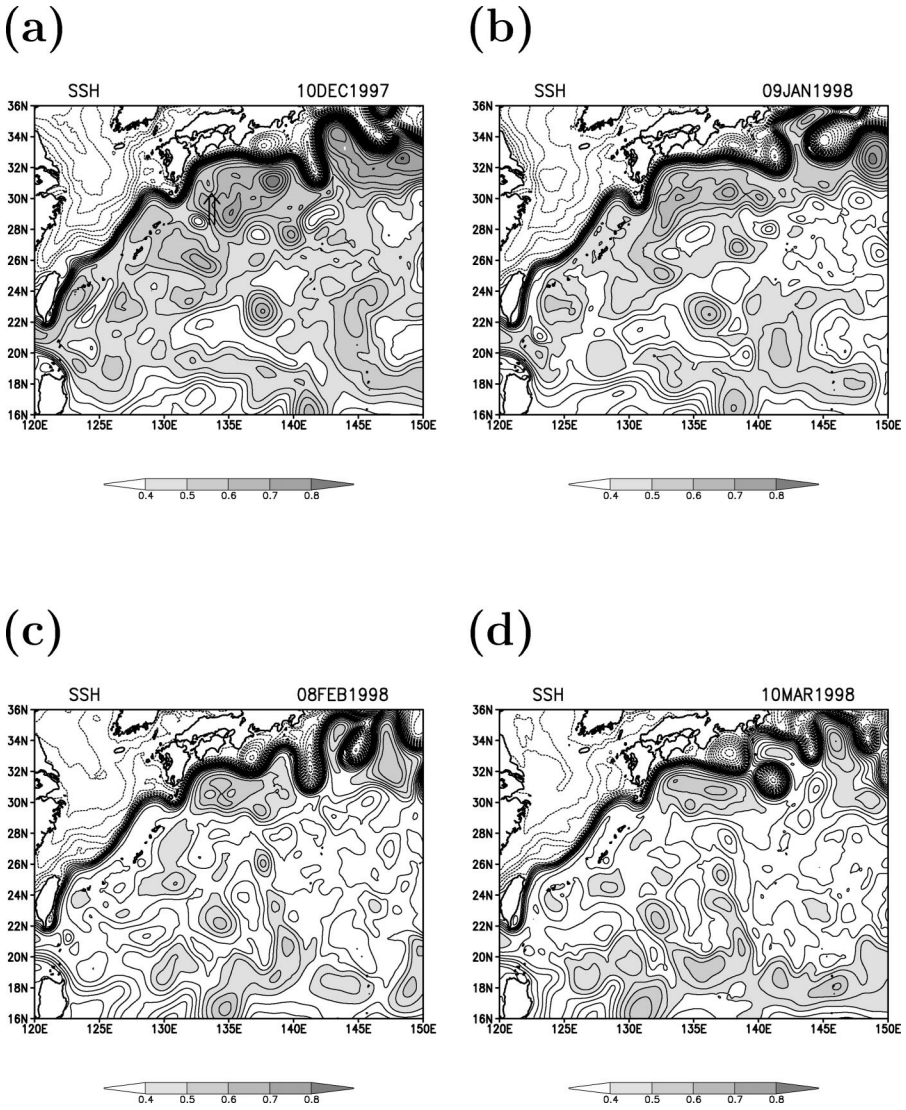

FIG. 11. As in Fig. 10 except showing the amplification of the Kuroshio meander due to the interaction with the cyclonic eddy [indicated by an arrow in (a)]: (a) 10 Dec 1997, (b) 9 Jan 1998, (c) 8 Feb 1998, and (d) 10 Mar 1998.

of the meander because the maximum of the eddy kinetic energy on the offshore side at 32.7°N (Fig. 14a) is accompanied only by the maximum in *K*. The energetics for the other large meander path show similar features (not shown).

Time series of both vertical and horizontal velocity shear averaged along the Kuroshio main stream show that the vertical shear of the Kuroshio increases prior to the onset of the large meander (Fig. 15). This leads to enhancement of the baroclinicity. The horizontal shear of the Kuroshio also increases prior to the large meander path, leading to a favorable condition for barotropic instability. Those preconditions permit the Kuroshio to generate the meander through the interaction with finite-amplitude disturbances, that is, mesoscale eddies. Zhu et al. (2001) also observed increase of both vertical and horizontal shear of the Kuroshio south of Shikoku prior to the path transition from the nearshore to the offshore nonlarge meander during the period from 1994 to 1995.

We, therefore, analyze the stability of the preconditioned Kuroshio using a two-dimensional inviscid primitive equation model (cf. Xue and Mellor 1993). The preconditioned velocity profile from 31° to 33.5°N at 136°E is used for the analysis. The bottom topography and the velocity profile are approximated using the analytical functions as described in the appendix. Figure 16 shows the growth rate and the phase speed for the unstable modes corresponding to the above two meanders. The most preferred mode has an *e*-folding time of 3.0–3.4 days and wavelength of 240–260 km. The phase speed for the most unstable wave is 35 km day^{-1}

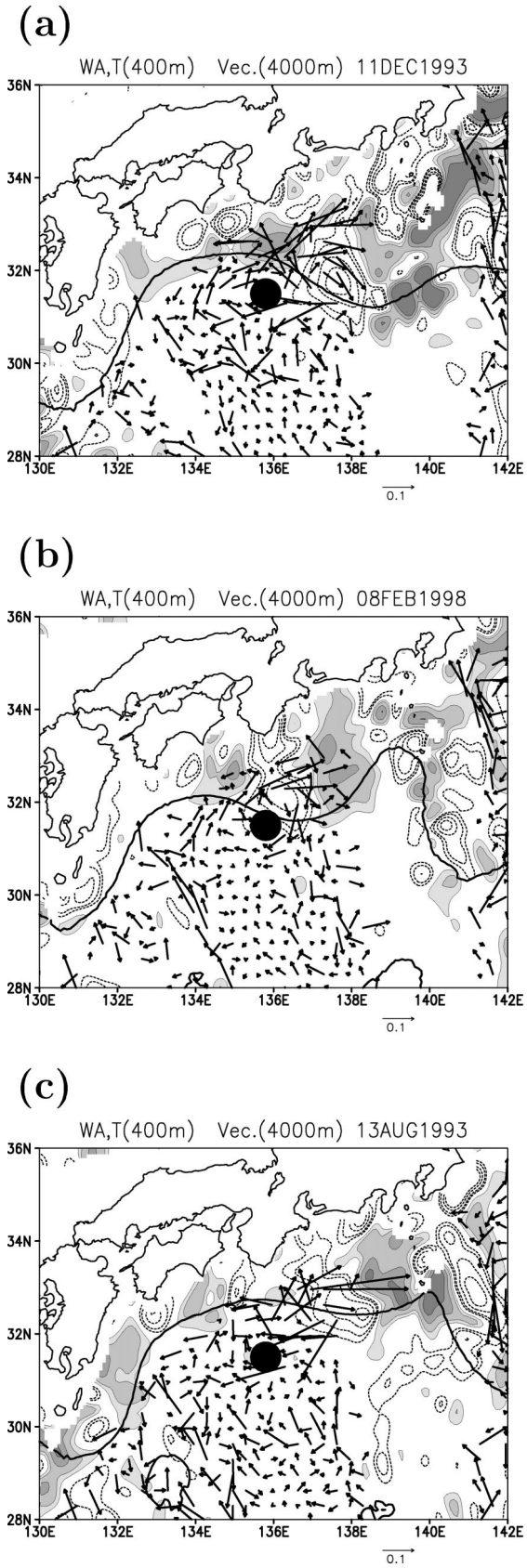

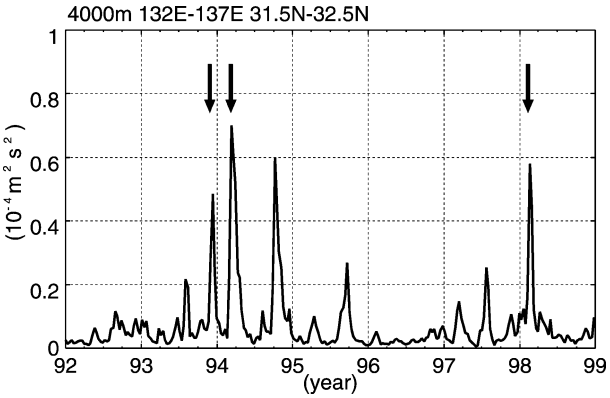

FIG. 13. Time series of kinetic energy ($m^2\ s^{-2}$) at 4000-m depth averaged over 31.5°–32.5°N, 132°–137°E.

and does not show significant dependence on the downstream wavenumber. Characteristics of the most unstable mode are summarized in Table 2. The energetics of the unstable mode are calculated using the baroclinic conversion term *P*, the buoyancy term *B*, and the barotropic conversion term *K*. As shown in Table 2, the ratios of *B* and *K* to *P* show that baroclinic energy transfer is mainly responsible for the growth of the unstable wave.

Similar characteristics of the meander simulated by the OGCM were estimated from the sequences of sea surface height (Table 3). The simulated meander grows and moves more slowly than expected from the linear stability analysis. The wavelength is larger than the theoretical prediction. The finite amplitude of the meander and the existence of viscosity in the OGCM may be responsible for these differences. This is because the structure of the unstable disturbance corresponds well to that of the simulated disturbance near 33°N in the OGCM (Fig. 17a). The vertical structures for the barotropic conversion term *K* and the baroclinic conversion *P* are also similar to those near 33°N in the OGCM (Figs. 17b,c). The ratio *K*/*P* estimated in the onshore region for the OGCM (Table 3) also indicates that the baroclinic instability dominates in the onshore side during the initial growth. On the other hand, barotropic instability is responsible for the growth in the offshore region (Table 3).

To check the parameter dependence of the above re-

←

FIG. 12. Snapshots of the smoothed vertical velocity at 400-m depth: (a) the large meander case on 13 Aug 1993, (b) the large meander case on 21 Mar 1994, and (c) the offshore nonlarge meander case on 8 Feb 1998. The shaded region denotes upwelling, and the dashed contour denotes downwelling. Koshu Seamount is indicated by a closed circle in each panel. Contour interval is −0.03, −0.02, −0.01, −0.005, 0.005, 0.01, 0.02, and 0.03 cm s^{-1}. The horizontal velocity at 4000-m depth is also shown by the vectors. To show the Kuroshio path, the temperature contour of 13°C at 400-m depth is denoted by the thick line.

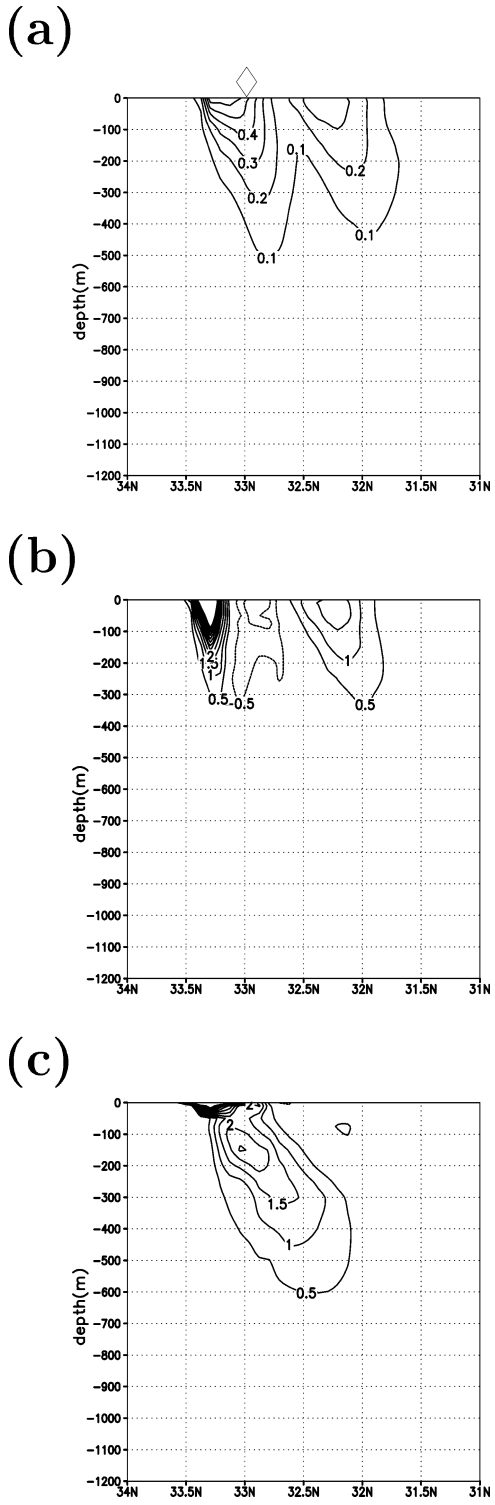

FIG. 14. Depth–latitude sections at 136°E for (a) time-mean eddy kinetic energy (contour interval is 0.1 $m^2\ s^{-2}$), (b) time-mean barotropic conversion (contour interval is $0.5 \times 10^{-6}\ m^2\ s^{-3}$), and (c) time-mean baroclinic conversion (contour interval is $0.5 \times 10^{-6}\ m^2\ s^{-3}$). The period of time mean is from 2 Oct 1993 to 10 Jan 1994. The diamond at the top of (a) indicates mean position of the Kuroshio.

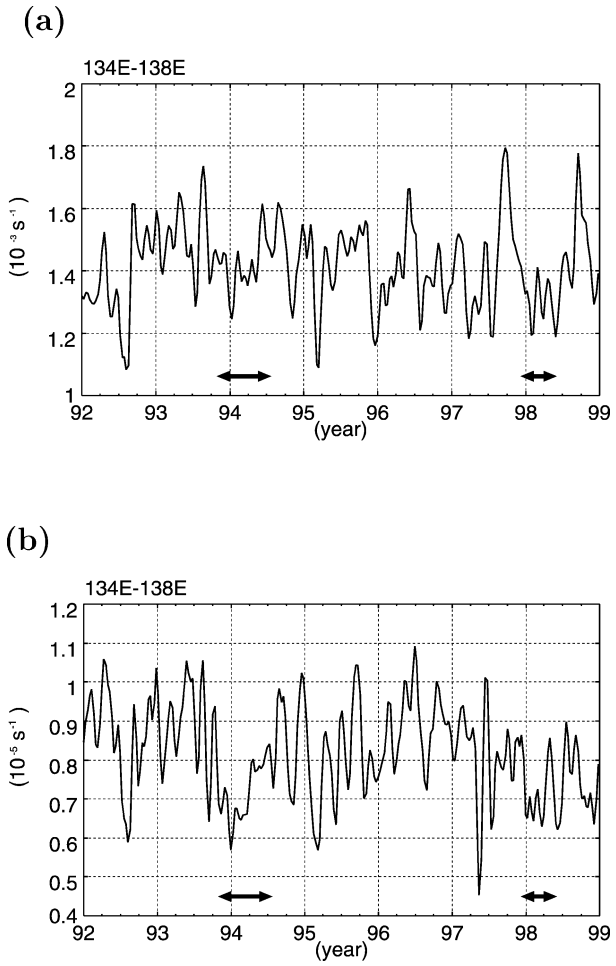

FIG. 15. Time series of the rms velocity shear of the Kuroshio main stream in 134°–138°E from 100 to 1000 m. The Kuroshio main stream is defined as the region in which mean velocity is greater than 0.4 m s^{-1}. Variations with time scale shorter than 30 days are removed. (a) Vertical shear, and (b) horizontal shear.

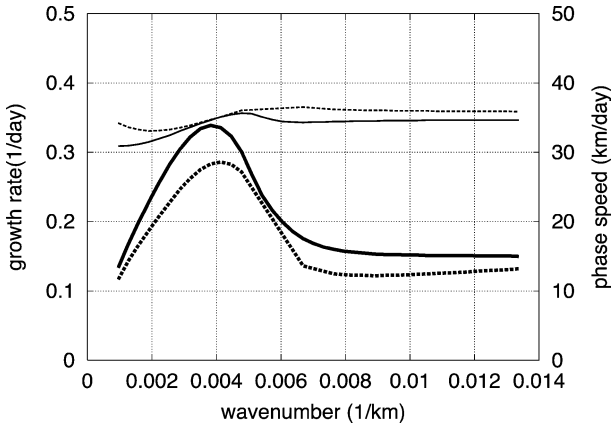

FIG. 16. Growth rate and phase speed for the velocity profiles at 136°E on 12 Oct 1993 (solid line) and 9 Jan 1998 (dashed line). Thick lines denote growth rate, and thin lines denote phase speed.

TABLE 2. Characteristics of the most unstable wave for two velocity profiles: *B/P* denotes the ratio of the buoyancy term *B* to the baroclinic conversion term *P*, and *K/P* denotes the ratio of the barotropic conversion term to the baroclinic conversion term *P*.

Profile on	Growth rate (day^{-1})	Phase speed (km day^{-1})	Wavelength (km)	*K/P*	*B/P*
12 Oct 1993	3.4×10^{-1}	35	260	0.120	0.863
9 Jan 1998	2.9×10^{-1}	35	240	0.077	0.875

sults, we have analyzed several other profiles obtained by perturbing parameters defining the velocity profile by one standard deviation during the simulation period (Fig. 18). It is found that lower current speed smaller $\overline{U}_0$), lower vertical shear (larger Z_s), shifting the velocity core more toward the coast (smaller y_f), broader current width (smaller y_{d1}, y_{d2}) and more southward inclination of the velocity core (larger A_0) lead to reduction of the growth rate. In particular, shifting the velocity core toward the coast by 30 km remarkably stabilizes the current. This is because the bottom slope constrains the baroclinic energy transfer (De Szoeke 1975). The offshore position of the model Kuroshio is highly sensitive to the interaction with offshore eddies just before the meanders occur (not shown). This suggests that the Kuroshio can be preconditioned by the eddies through the offshore shift of the main axis.

d. Variation of the Kuroshio recirculation

The present analysis of the model results suggests that the preconditioned Kuroshio may generate the large meander path through baroclinic instability triggered by either an anticyclonic or a cyclonic eddy. According to Kagimoto and Yamagata (1997), the anticyclonic Kuroshio recirculation is intensified by a merger of anticyclonic eddies. Therefore we discuss roles of the Kuroshio recirculation at the preconditioning phase. To achieve this, analysis of the vorticity budget is useful.

The vorticity budget is calculated using the following equation (Ezer and Mellor 1994; Kagimoto and Yamagata 1997):

TABLE 3. Characteristics of the meanders simulated by the OGCM: *K/P* in the onshore region denotes the ratio of the barotropic conversion term to the baroclinic conversion term *P* in 32.5°–33.5°N, 135°–136°E, and *K/P* denotes that in 31.0°–33.5°N, 135°–136°E.

Meander	Growth rate (day^{-1})	Phase speed (km day^{-1})	Wavelength (km)	*K/P* in the onshore region	*K/P*
Oct 1993	0.7×10^{-1}	12	600	0.208	0.655
Jan 1998	0.7×10^{-1}	6	720	0.221	0.427

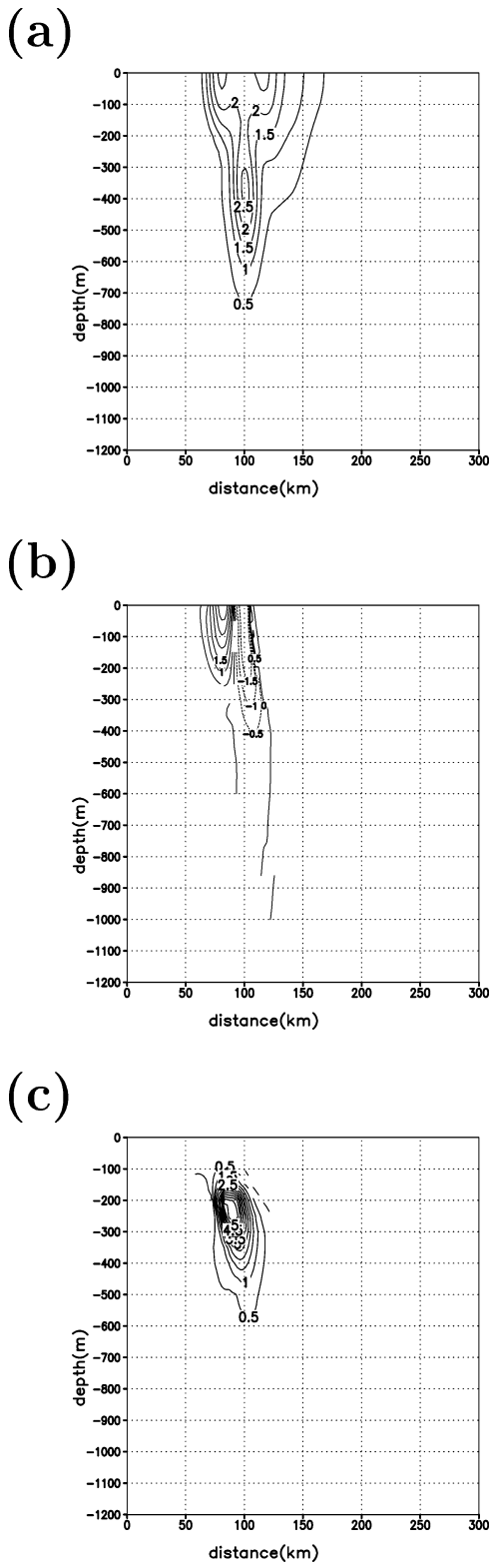

FIG. 17. Depth–latitude sections at 136°E for (a) structure of the growing disturbances ($\tilde{u}^2 + \tilde{v}^2$), (b) barotropic conversion, and (c) baroclinic conversion.

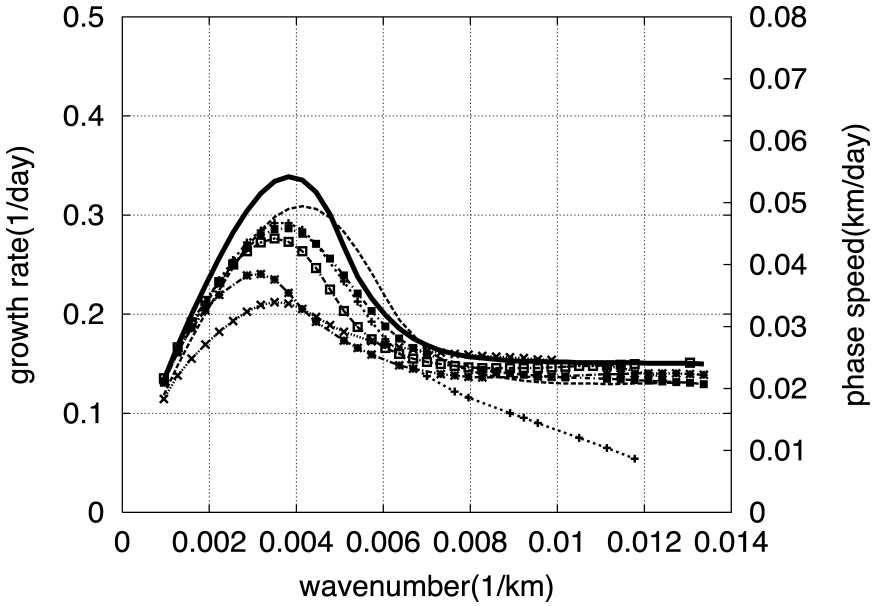

FIG. 18. Dependence of the growth rate on various velocity profiles at 136°E on 12 Oct 1993 for $U_0 = 1.4$ m s^{-1} (dashed line), $Z_s = 710$ m (dashed line with pluses), $y_f = 80$ km (short dashed line with crosses), $y_{d1} = 49$ km (dash–dotted line with asterisks), $y_{d2} = 49$ km (dash–dotted line with open squares), and $A_0 = 4.4$ (dash–dotted line with closed squares). Thick solid line denotes the basic growth rate.

$$\frac{\partial}{\partial t}\left[\frac{\partial(\overline{v}D)}{\partial x} - \frac{\partial(\overline{u}D)}{\partial y}\right] = -\left(\frac{\partial A_y}{\partial x} - \frac{\partial A_x}{\partial y}\right) - \left[\frac{\partial(f\overline{u}D)}{\partial x} + \frac{\partial(f\overline{v}D)}{\partial y}\right] + J(P_b, D) + \text{curl}(\tau_s - \tau_b), \quad (3)$$

where D is the depth, $(\overline{u}, \overline{v})$ are the vertical averaged velocities, (A_x, A_y) are the vertically integrated advection plus diffusion terms in the zonal and the meridional momentum equations, respectively, f is the Coriolis parameter, P_b is the bottom pressure, and τ_s and τ_b are the wind and the bottom stresses, respectively; J denotes the Jacobian operator. The term on the left-hand side is the vorticity tendency term, and the terms on the right-hand side are the advection plus diffusion of the vorticity, the planetary geostrophic divergence, the bottom pressure torque, and the curl of wind and bottom stresses. The second term on the right-hand side of Eq. (3) is reduced to the planetary beta effect when the time dependence of the surface elevation is negligible (Kagimoto and Yamagata 1997).

Figure 19a shows the time series of vorticity ($\partial\overline{v}D/\partial x - \partial\overline{u}D/\partial y$) averaged in the Kuroshio recirculation region (30°–33°N, 133°–140°E). The area-averaged anticyclonic (i.e., negative) vorticity is significantly intensified just before the occurrence of the large meander. The anticyclonic vorticity averaged in the area excluding the cyclonic meander region shows a more drastic variation. The time evolution of all terms in (3) is shown in Fig. 19b. We note that diffusion is negligible in comparison with advection; the wind stress is negligible in comparison with the bottom stress in this region.

During the nonlarge meander period, the negative beta advection and nonlinear advection terms are almost balanced with the positive bottom pressure and stress torques. This suggests that the Kuroshio interacts with the bottom slope through bottom pressure torque during the period. The advection intensifies the anticylonic vorticity during the nonlarge meander period; each negative peak of the advection term corresponds to intrusion of anticylonic eddies. In particular, the anticyclonic vorticity is supplied by the advection from the summer of 1992 to autumn of 1993 in the model.

When the first large meander occurs, the balance among terms drastically changes. The beta advection term changes from a negative value to a positive value owing to the strong southward flow. The nonlinear advection term and bottom stress torque frequently change sign owing to large variation of the cyclonic meander and the anticylonic recirculation. Because of the lack of constant supply, the anticyclonic vorticity in the recirculation region weakens during the large meander period. The second large meander occurs after the anticyclonic vorticity is again significantly intensified in the summer of 1997.

The time series of the model Kuroshio volume transport across the PN and ASUKA lines suggests a cause of the intensification of the Kuroshio recirculation (Fig. 20). The volume transport across the PN line increases

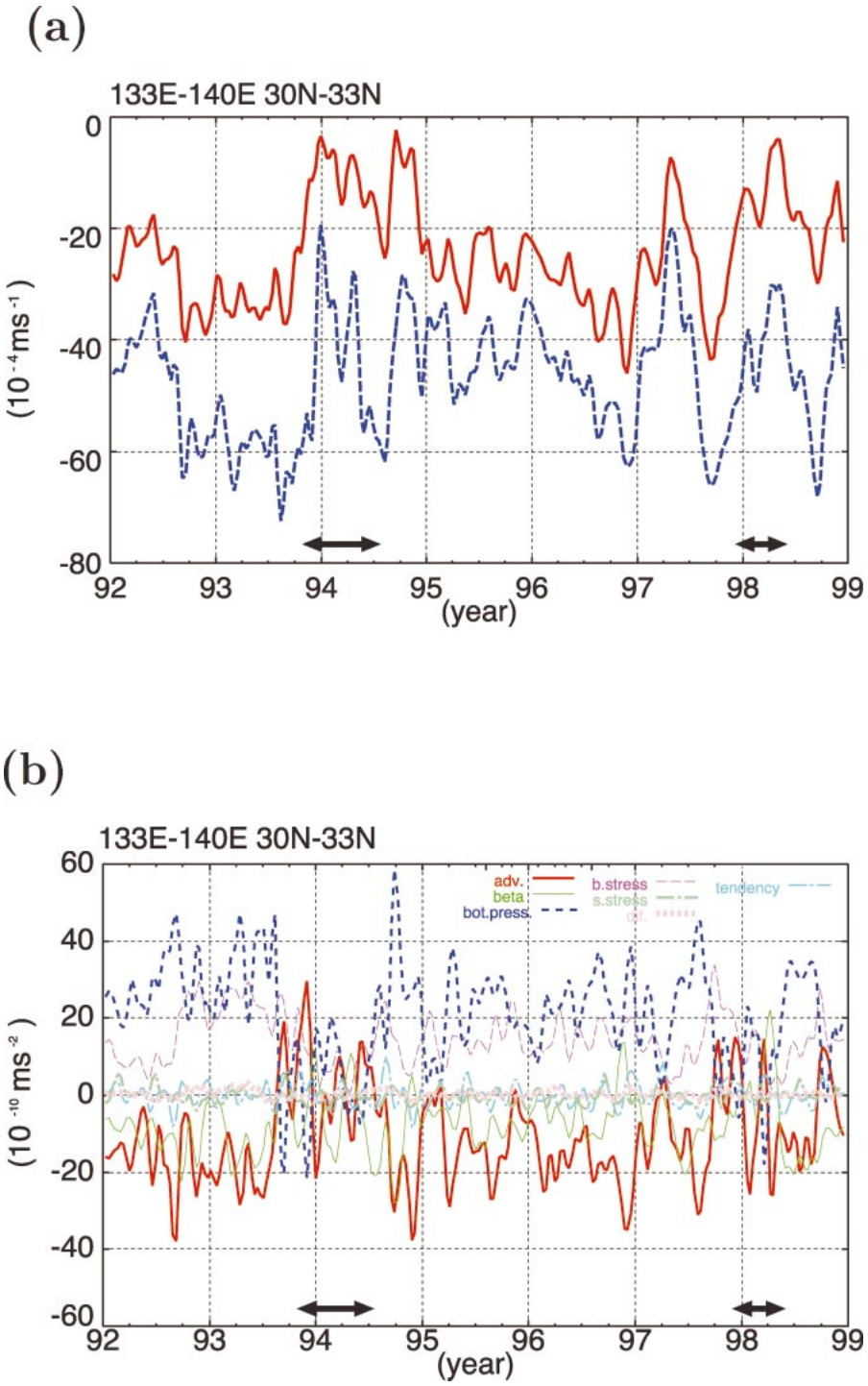

FIG. 19. (a) Time series of mean vorticity of vertically integrated velocities in 30°–33°N, 133°–140°E (solid line). Dashed line denotes mean vorticity in the area excluding the Kuroshio meander. Variations with time scale shorter than 30 days are removed. (b) Time series of torque balance in 30°–33°N, 133°–140°E. Variations with time scale shorter than 30 days are removed.

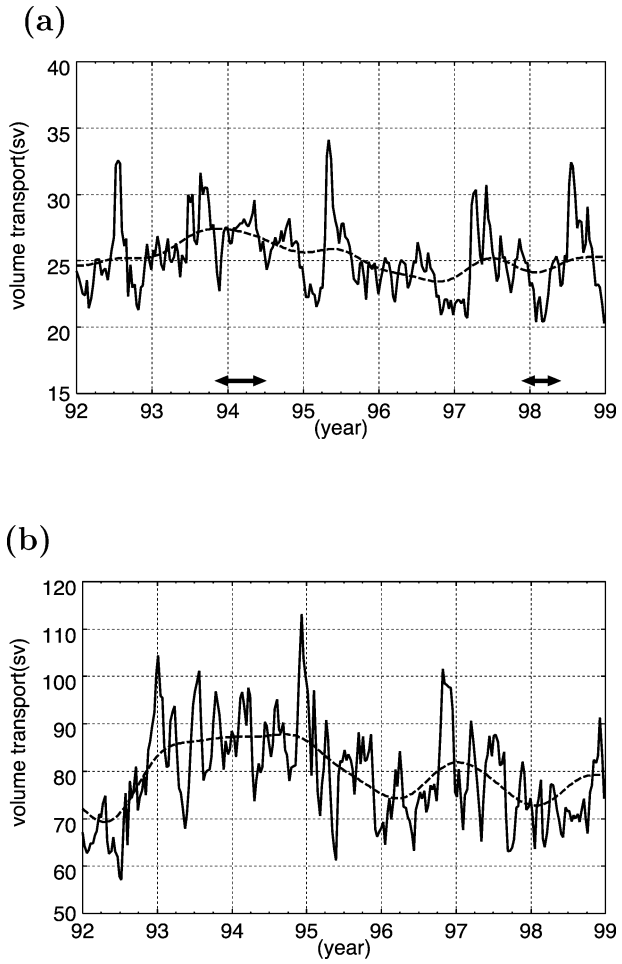

FIG. 20. Time series of the model Kuroshio transport across (a) the PN line relative to 700 m and (b) the ASUKA line upper 1000 m from 1992 to 1998. Thin line denotes the filtered estimate (longer than 1 yr) of the volume transports.

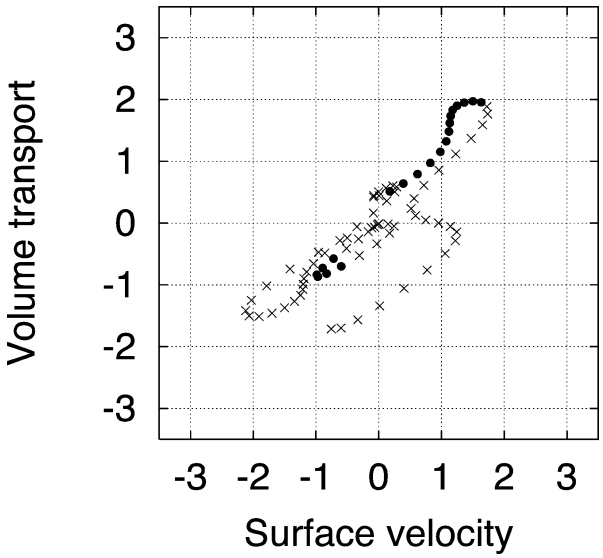

FIG. 21. Relations between the surface velocity of the Kuroshio (in the Tokara Strait) and the volume transport (across the PN line). Closed circles correspond to the large meander and crosses correspond to the nonlarge meander. The unit is one standard deviation from the mean. The surface velocity in the Tokara Strait is estimated from the sea level difference between Naze and Nishinoomote (1 and 2 in Fig. 1, respectively).

seasonally when the anticyclonic eddies pass through the PN line in summer (Kagimoto and Yamagata 1997). The interannual increase of the Kuroshio volume transport across the PN line during the period from 1993 to 1994 and the period from 1997 to 1998 is also due to the interannual enhancement of the eddy activity. Since the anticyclonic eddies intrude into the Kuroshio recirculation region and circulates in the region (see Fig. 9), the volume transport across the ASUKA line is highly variable. The intensification of the anticyclonic Kuroshio recirculation corresponds to the merger of anticyclonic eddies traced back to the region northeast of Luzon Island (e.g., Fig. 9a). In 1995, the recirculation is reduced by the intrusion of a cyclonic eddy despite the merger of the anticylonic eddies from the upstream region.

Both theoretical and observational studies (e.g., White and McCreary 1976; Kawabe 1995) suggest that the Kuroshio path south of Japan is related to variation of the volume transport and the surface velocity at upstream locations, for example, the PN line. Figure 21 shows relations among the Kuroshio volume transport, the surface velocity, and the Kuroshio meander from the present model. The large meander is basically associated with large transport and large surface velocity on an interannual time scale. This is consistent with another model result, Kagimoto (1999), and supports the relation obtained from observations (Kawabe 1995). This typical tendency corresponds to the first meander from November 1993 to July 1994. However, the large meander exists even when the transport and surface velocity are near normal. The latter case corresponds to the second meander from January 1998 to May 1998. We suggest that the supply of anticyclonic eddies from the upstream region as shown by the increase of the volume transport in 1997 destabilizes the Kuroshio prior to the second meander (Fig. 20a).

5. Summary and discussion

We have discussed the results from the OGCM experiment for the period from 1992 through 1998 using the high-resolution nested grid model for the North Pacific. It has turned out that the present model successfully reproduces several important features. Those features are 1) the propagation of anticyclonic eddies and their merger with the Kuroshio recirculation in the Shikoku Basin, 2) frequent occurrence of the offshore nonlarge meander owing to the interaction between the Kuroshio and the anticyclonic eddy, 3) the intensification of the Kuroshio recirculation (identified by the increase

of volume transports across the ASUKA lines) due to supply of anticyclonic vorticity prior to the large meander, 4) the large meander triggered by the interaction between the anticyclonic eddy and the strong Kuroshio recirculation, 5) the initial growth of the large meander due to the baroclinic instability, and 6) the demise of the meander after shedding the cyclonic ring intensified by the merger of the cyclonic eddy.

A synthesis of these results leads to the following scenario for the formation of the Kuroshio large meander. At the beginning, anticyclonic eddies are activated near Taiwan or the Philippine coast and advected by the Kuroshio into the Shikoku Basin. The transport across the PN line increases by the successive arrival of those anticyclonic eddies and the anticyclonic Kuroshio recirculation south of Shikoku is intensified by the merger of those eddies. Then, the Kuroshio large meander is generated by baroclinic instability triggered by the interaction with the anticyclonic/cyclonic eddies. During the meandering period, the meandering cyclonic jet matures by absorbing a cyclonic ring propagating from the Kuroshio Extension and eventually sheds the cyclonic ring. Thus, the large meander state ends. The above scenario suggests the importance of eddy activities to the Kuroshio meandering and provides a key to predict the ever-mysterious phenomenon of the Kuroshio meander; the eddy activities introduce a favorable condition for the Kuroshio large meander through intensification of the Kuroshio recirculation.

So far, observational studies have suggested that the Kuroshio large meander occurs through generation of a small meander southeast of Kyushu [so-called trigger meander according to Solomon (1978)]. The present model shows that the anticyclonic/cyclonic eddies propagate westward along 29°–32°N (see Fig. 6d) and interact directly with the Kuroshio south of Shikoku. Since the actual eddies may interact with the Kuroshio southeast of Kyushu, the concept of the trigger meander might have captured this possible phenomenon (Endoh and Hibiya 2001).

The simulated large meander does not persist long and it changes into the offshore nonlarge meander. The meander east of the Izu–Ogasawara Ridge and the cyclonic eddy south of the Kuroshio Extension influence the stability of the large meander in the model (see Figs. 10 and 11). This study suggests that the persistence of the Kuroshio large meander is strongly affected by the mesoscale eddies generated by flow instabilities. Ichikawa and Imawaki (1994) reported the merger of the Kuroshio large meander and the cyclonic eddy originated from the Kuroshio Extension using *Geosat* data. They did not clarify how this event influenced the amplitude of the large meander. More intensive observational studies are certainly needed to clarify the interaction of mesoscale eddies with the Kuroshio path variation.

In the present simulation, the Kuroshio large meander occurs through intensification of the Kuroshio recirculation caused by the interannual variation of the Kuroshio transport across the PN line. The volume transport of the Kuroshio increases through amplification of the anticyclonic eddies originated in the region near the Luzon Island as indicated by the local maximum of the EKE there (Fig. 5b; also see Figs. 9a,d). More detailed analysis of eddy activity near Luzon Island is certainly necessary. We note that the simulated eddy activity from the subtropical front east of the Nansei Islands is weaker than in the observations (Fig. 5). Since mesoscale eddies in this region are important to generate the variation of the Kuroshio volume transport (Ichikawa 2001), improvement of the model performance in this region may lead to a more realistic simulation of the Kuroshio path variation.

Acknowledgments. We appreciate useful discussions with Drs. H. Hukuda and T. Kagimoto during the course of the present work. Dr. H. Xue kindly provided us with the code for the linear stability analysis. We are also thankful to two referees and, in particular, the editor Dr. L. D. Talley for their constructive comments on the earlier version of the manuscript. This work is part of the Japan Coastal Ocean Predictability Experiment (JCOPE) started in October 1997 under the initiative of the Frontier Research System for Global Change (FRSGC), which is supported jointly by National Space Development Agency of Japan (NASDA) and Japan Marine Science and Technology Center (JAMSTEC). The scientific interaction with the IOC/UNESCO NEAR-GOOS project supported by Ministry of Education, Culture, Sports, Science and Technology (MEXT) was helpful in completing this work.

APPENDIX

Linear Stability Analysis

Linear instability of the velocity profile of the Kuroshio is investigated using a two-dimensional, inviscid primitive equation model (cf. Xue and Mellor 1993) to clarify mechanisms of the initial growth of the meander. The governing equations for the disturbances are

$$\frac{\partial u}{\partial t} + U\frac{\partial u}{\partial x} - fv + v\frac{\partial U}{\partial y} + w\frac{\partial U}{\partial z} + \frac{1}{\rho_0}\frac{\partial p}{\partial x} = 0,$$

$$\frac{\partial v}{\partial t} + U\frac{\partial v}{\partial x} + fu\frac{1}{\rho_0}\frac{\partial p}{\partial y} = 0,$$

$$b - \frac{1}{\rho_0}\frac{\partial p}{\partial z} = 0,$$

$$\frac{\partial u}{\partial x} + \frac{\partial v}{\partial y} + \frac{\partial w}{\partial z} = 0, \quad \text{and}$$

$$\frac{\partial b}{\partial t} + U\frac{\partial b}{\partial x} + v\frac{\partial B}{\partial y} + w\frac{\partial B}{\partial z} = 0, \quad \text{(A1)}$$

where u, v, and w represent x, y, and z components

of the perturbation velocity vector; p is the perturbation pressure; and b is the perturbation buoyancy, $b = -g\rho(y, z)/\rho_0$. A steady current $U(y, z)$ is assumed to flow parallel to the coast, which is in thermal wind balance; for example, $fU_z = B_y$, where subscripts indicate partial derivatives. The boundary conditions are

$$\begin{aligned} v &= 0 && \text{at } y = 0, \\ p, u, v &\to 0 && \text{at } y \to \infty, \\ w &= 0 && \text{at } z = 0, \quad \text{and} \\ w &= -v(\partial h/\partial y) && \text{at } z = -h(y). \end{aligned} \tag{A2}$$

For later convenience, we introduce a bottom-following coordinate:

$$\varsigma = 1 + \frac{z}{h(y)}. \tag{A3}$$

Then the vertical velocity is transformed into

$$\omega = w - (\varsigma - 1)v\frac{\partial h}{\partial y}. \tag{A4}$$

We assume perturbed disturbances of the form

$$\begin{aligned} u &= \mathrm{Re}\{\tilde{u}(y, \zeta) \exp[i(\sigma t + lx)]\}, \\ v &= \mathrm{Re}\{i\tilde{v}(y, \zeta) \exp[i(\sigma t + lx)]\}, \\ u &= \mathrm{Re}\{\tilde{\omega}(y, \zeta) \exp[i(\sigma t + lx)]\}, \\ b &= \mathrm{Re}\{i\tilde{b}(y, \zeta) \exp[i(\sigma t + lx)]\}, \quad \text{and} \\ p &= \mathrm{Re}\{i\tilde{p}(y, \zeta) \exp[i(\sigma t + lx)]\}, \end{aligned} \tag{A5}$$

where l is the downstream wavenumber and $\sigma = \sigma_r + i\sigma_i$ is the frequency. The above system is solved by the spectral technique. It has turned out that a truncation level of 28 is sufficient to obtain a convergent solution. Interested readers are referred to Xue and Mellor (1993) for details of the spectral technique.

In the present analysis, the meridional section of Kuroshio from 31° to 33.5°N at 136°E is adopted. The bottom topography including a sharp continental slope is approximated by the following function (Xue and Mellor 1993):

$$h(y) = H_s + \frac{1}{2}(H_d - H_s)\left(1 + \tanh\frac{y - y_m}{\alpha}\right), \tag{A6}$$

where H_s and H_d are the minimum depth and the maximum depth in the domain, respectively. The slope is given by α and the maximum slope is realized at $y = y_m$. The four parameters (H_s, H_d, α, y_m) are given by 1110 m, 4600 m, 20 km, and 80 km, respectively; they are determined by the least squares method from the model topography. The background velocity profile is given by the following formula as in Xue and Mellor (1993):

TABLE A1. Parameters of two velocity profiles.

Profile on	U_0 (m s^{-1})	Z_s (m)	y_f (km)	y_{d1} (km)	y_{d2} (km)	A_0
12 Oct 1993	1.60	650	110	36	74	3.5
9 Jan 1998	1.38	655	100	34	66	4.3

$$\begin{aligned} U(y, z) &= U_0 \exp\left(\frac{z}{z_s} - Y_i^2\right), \\ Y_i &= Y_i(y) = \left[y - y_f\left(1 - \frac{z}{z_s A}\right)\right]\frac{1}{y_d}, \\ A &= A_0 + 2\frac{z}{H_d}, \quad \text{and} \\ y_d &= \begin{cases} y_{d1} - \dfrac{z(y_{d2} - y_{d1})}{H_d} - \dfrac{y_{d2} - y_{d1}}{H_d}, & \text{if } Y_i \le 0 \\ y_{d2}, & \text{if } Y_i > 0, \end{cases} \end{aligned} \tag{A7}$$

where U_0 is the maximum velocity of the Kuroshio, y_f is the distance of the location of the surface velocity maximum from the northern boundary, y_d is the width of the Kuroshio, z_s is the velocity decreasing rate against depth, and A is the southward tilt of the maximum velocity with increasing depth. The above six parameters (U_0, z_s, y_f, y_{d1}, y_{d2}, A_0) are determined by the least squares method for the 10-day mean velocity data just before the meander occurs. Parameters on 12 October 1993 and 9 January 1998 are summarized in Table A1.

REFERENCES

Akitomo, K., and M. Kurogi, 2001: Path transition of the Kuroshio due to mesoscale eddies: A two-layer, wind-driven experiment. *J. Oceanogr.*, **57,** 735–741.

Boyer, T. P., and S. Levitus, 1997: Objective Analysis of Temperature and Salinity for the World Ocean on a 1/4 Degree Grid. World Ocean Atlas 1994, NOAA Atlas NESDIS 11, 62 pp.

Da Silva, A., C. Young, and S. Levitus, 1994: *Algorithms and Procedures.* Vol. 1, *Atlas of Surface Marine Data,* NOAA Atlas NESDIS 6, 83 pp.

De Szoeke, R. A., 1975: Some effects of bottom topography on baroclinic instability. *J. Mar. Res.*, **33,** 93–122.

Ebuchi, N., and K. Hanawa, 2000: Mesoscale eddies observed by TOLEX-ADCP and TOPEX/Poseidon altimeter in the Kuroshio recirculation region south of Japan. *J. Oceanogr.*, **56,** 43–57.

——, and ——, 2003: Influence of mesoscale eddies on variations of the Kuroshio path south of Japan. *J. Oceanogr.*, **59,** 25–36.

Emery, W. J., W. G. Lee, and L. Magaard, 1984: Geographical and seasonal distributions of Brunt–Väisälä frequency and Rossby radii in the North Pacific and North Atlantic. *J. Phys. Oceanogr.*, **14,** 294–317.

Endoh, T., and T. Hibiya, 2001: Numerical simulation of the transient response of the Kuroshio leading to the large meander formation south of Japan. *J. Geophys. Res.*, **106,** 26 833–26 850.

Ezer, T., and G. L. Mellor, 1994: Diagnostic and prognostic calculations of the North Atlantic circulation and sea level using a sigma coordinate ocean model. *J. Geophys. Res.*, **99,** 14 159–14 171.

Guo, X., H. Hukuda, Y. Miyazawa, and T. Yamagata, 2003: A triply nested ocean model simulating the Kuroshio–Roles of horizontal resolution of JEBAR. *J. Phys. Oceanogr.,* **33,** 146–169.

Haney, R., 1971: Surface thermal boundary condition for ocean circulation models. *J. Phys. Oceanogr.,* **1,** 241–248.

Hasunuma, K., and K. Yoshida, 1978: Splitting of the subtropical gyre in the western North Pacific. *J. Oceanogr. Soc. Japan,* **34,** 160–172.

Hurlburt, H. E., A. J. Wallcraft, W. J. Schmitz Jr., P. J. Hogan, and E. J. Metzger, 1996: Dynamics of the Kuroshio/Oyashio current system using eddy-resolving models of the North Pacific Ocean. *J. Geophys. Res.,* **101,** 941–976.

Ichikawa, K., 2001: Variation of the Kuroshio in the Tokara Strait induced by mesoscale eddies. *J. Oceanogr.,* **57,** 55–68.

——, and S. Imawaki, 1994: Life history of a cyclonic ring detached from the Kuroshio Extension as seen by the *Geosat* altimeter. *J. Geophys. Res.,* **99,** 15 953–15 966.

Imawaki, S., U. Hiroshi, H. Ichikawa, M. Fukazawa, S. Umatani, and ASUKA Group, 2001: Satellite altimeter monitoring the Kuroshio transport south of Japan. *Geophys. Res. Lett.,* **28,** 17–20.

Kagimoto, T., 1999: Numerical study on transport variations of the Kuroshio. Ph.D. thesis, The University of Tokyo, 75 pp.

——, and T. Yamagata, 1997: Seasonal transport variations of the Kuroshio: An OGCM simulation. *J. Phys. Oceanogr.,* **27,** 403–418.

Kawabe, M., 1985: Sea level variations at the Izu islands and typical stable paths of the Kuroshio. *J. Oceanogr. Soc. Japan,* **41,** 307–326.

——, 1987: Spectral properties of sea level and time scales of Kuroshio path variations. *J. Oceanogr. Soc. Japan,* **43,** 111–123.

——, 1995: Variations of current path, velocity, and volume transport of the Kuroshio in relation with the large meander. *J. Phys. Oceanogr.,* **25,** 3103–3117.

Levitus, S., and T. P. Boyer, 1994: *Temperature*. Vol. 4, *World Ocean Atlas 1994,* NOAA Atlas NESDIS **4,** 117 pp.

——, R. Burgett, and T. P. Boyer, 1994: *Salinity*. Vol. 3, *World Ocean Atlas 1994,* NOAA Atlas NESDIS **3,** 99 pp.

Masina, S., S. G. H. Philander, and A. B. G. Bush, 1999: An analysis of tropical instability waves in a numerical model of the Pacific Ocean 2. Generation and energetics of the waves. *J. Geophys. Res.,* **104,** 29 637–29 661.

Mellor, G. L., 1996: Users guide for a three-dimensional, primitive equation, numerical ocean model. [Available online at http://www.aos.princeton.edu/WWWPUBLIC/htdocs.pom/.]

——, and T. Yamada, 1982: Development of a turbulence closure model for geophysical fluid problems. *Rev. Geophys. Space Phys.,* **20,** 851–875.

——, T. Ezer, and L.-Y. Oey, 1994: The pressure gradient conundrum of sigma coordinate ocean models. *J. Atmos. Oceanic Technol.,* **11,** 1126–1134.

Mitsudera, H., T. Waseda, Y. Yoshikawa, and B. Taguchi, 2001: Anticyclonic eddies and Kuroshio meander formation. *Geophys. Res. Lett.,* **28,** 2025–2028.

Mizuno, K., and W. B. White, 1983: Annual and interannual variability in the Kuroshio current system. *J. Phys. Oceanogr.,* **13,** 1847–1867.

Qiu, B., and W. Miao, 2000: Kuroshio path variations south of Japan: Bimodality as a self-sustained internal oscillation. *J. Phys. Oceanogr.,* **30,** 2124–2137.

Reynolds, R. W., and T. M. Smith, 1994: Improved global sea surface temperature analysis. *J. Climate,* **7,** 929–948.

Robinson, A. R., and B. Taft, 1972: A numerical experiment for the path of the Kuroshio. *J. Mar. Res.,* **30,** 65–101.

Saiki, M., 1982: Relation between the geostrophic flux of the Kuroshio in the eastern China Sea and its large meanders in south of Japan. *Oceanogr. Mag.,* **32,** 11–18.

Smagorinsky, J., S. Manabe, and J. L. Holloway, 1965: Numerical results from a nine-level general circulation model of the atmosphere. *Mon. Wea. Rev.,* **93,** 727–768.

Solomon, H., 1978: Occurrence of small ''trigger'' meanders in the Kuroshio off southern Kyushu. *J. Oceanogr. Soc. Japan,* **34,** 81–84.

Stammer, D., 1997: Global characteristics of ocean variability estimated from regional TOPEX/Poseidon altimeter measurements. *J. Phys. Oceanogr.,* **27,** 1743–1769.

Wells, N. C., V. O. Ivchenko, and S. E. Best, 2000: Instabilities in the Agulhas retroflection current system: a comparative model study. *J. Geophys. Res.,* **105,** 3233–3241.

White, W. B., and J. P. McCreary, 1976: On the formation of the Kuroshio meander and its relationship to the large-scale ocean circulation. *Deep-Sea Res.,* **23,** 33–47.

Xue, H., and G. Mellor, 1993: Instability of the Gulf Stream meanders in South Atlantic Bight. *J. Phys. Oceanogr.,* **23,** 2326–2350.

Yamagata, T., and S. Umatani, 1987: The capture of current meander by coastal geometry with possible application to the Kuroshio current. *Tellus,* **39A,** 161–169.

——, Y. Shibao, and S. Umatani, 1985: Interannual variability of the Kuroshio Extension and its relation to the Southern Oscillation/El Nino. *J. Oceanogr. Soc. Japan,* **41,** 274–281.

Zhu, X.-H., A. Kaneko, T. Saito, and N. Gohda, 2001: Kuroshio stream path variation and its associated velocity structures south of Shikoku, Japan. *Geophys. Res. Lett.,* **28,** 4615–4618.

——, I.-S. Han, J.-H. Park, H. Ichikawa, K. Murakami, A. Kaneko, and A. Ostrovskii, 2003: The Northeastward current southeast of Okinawa Island observed during November 2000 to August 2001. *Geophys. Res. Lett.,* **30,** 1071, doi:10.1029/2002GL015867.